Flexible DC distribution network fault protection method based on transient characteristics differences of fault current

Zhi-hui Zeng[a], Jia-yin Li[a], Yan-fang Wei[a], Xiao-wei Wang[c], Ying-ying Zheng[a]

[a] *School of Electrical Engineering and Automation, Henan Polytechnic University, Jiaozuo 454003, China;*

[c] *School of Electrical Engineering, Xi'an University of Technology, Xi'an 710000, China*

Abstract: To improve the rapidity and accuracy of fault detection in multi-terminal flexible DC distribution networks with modular multilevel converters. A protection method based on the transient characteristic difference of fault current is proposed. First, the parameters of the complete ensemble empirical mode decomposition with adaptive noise (CEEMDAN) are optimized using the Aquila Optimizer algorithm. So that, the feature extraction effect is optimal. Secondly, the distinction in the magnitude of internal and external fault currents is deduced through detailed fault characterization. Thus, the energy moment eigenvalue of the fault current is used to construct the internal and external fault criterion. Then, depending on the distinction between the faulty and sound pole currents during internal fault. The ratio of the singular value of the positive and negative pole currents is taken to create the differentiation criterion of faulty pole. This protection scheme can reliably and sensitively recognize various types of short-circuit faults by only using DC line single-end current signals. Finally, the validity and robustness of this method are confirmed by simulating and analyzing under different working conditions.

Key words: Flexible DC distribution network, Fault analysis, Aquila Optimizer, Fault current, Energy moment, Singular value.

1. Introduction

As the percentage of clean energy in the energy system increases, the rational development and utilization of energy has become the key to solving China's resource and environmental problems. Flexible DC distribution network has the great transmission capacity, long transmission distance, low line loss, system stability and other characteristics. Therefore, flexible DC transmission technology has been widely used. And it has been a key research subject in the field of DC power transmission 0[2]. Relay protection is one of the important technical problems facing the development of flexible DC distribution network. When the network DC line failure, the fault current rises quickly, within a few milliseconds. That will threaten the safety of the entire power grid. Therefore, the relay protection scheme of power grid should have high rapidity and reliability [3]-[5].

1.1 Previous and Related Work

For Flexible DC distribution network transmission line protection, domestic and foreign scholars have done extensive studies. They mainly focusing on the identification of faulty feeder when transmission line fail. Since the fault current signal at this time contains a large amount of fault information, many scholars use signal processing techniques to collect fault signature for fault feeder identification. These include Wavelet transform (WT) [6]-[9], S-transform [10]-[12], Hilbert-Huang transform (HHT) [13]-[14], Prony algorithm [15]-[16], Mathematical morphology (MM) [17]-[18] and so on.

S et al. obtained the traveling wave arrival time by using continuous WT to predict the fault location [6]. Liu et al. proposed a fault localization method for MTDC system based on wavelet transform technique [7]. Literature [8] used a combination of boundary protection and traveling wave protection, processed the DC signals using synchro squeezed wavelet transform (SWT), and then used the wavelet modulus maximum to represent the traveling wave signals. Literature [9] applied WT to extract the transient voltages to identify faulty lines in a DC network. Xi et al used S-transform to extract the amplitude of the line mode traveling wave signal at each frequency component [10]. Literature [11] proposed the use of S-transform to obtain the S-amplitude matrix of the zero-sequence currents and compare the integrated amplitude difference. Literature [12] performed fault identification by ratio difference of transient voltage energy by S transform. Luo et al. used Hilbert transform to calculate reactive energy to discern fault [13].Hao et al. used HHT to capture fault characteristics [14]. Literature [15] used Prony algorithm to extract voltage and current at specified frequency to calculate input impedance for fault identification. Literature [16] proposed a fault diagnosis method is predicated upon Prony algorithm to obtain phase information at the injected frequency. Yu et al proposed a detection methodology where the algorithm divides the voltage sampling data into two parts by means of an allocation time chosen by MM. The ratio of the voltage integrals of the two parts is then utilized to detect faults [17]. Literature [18] modified the existing MM technique

*Corresponding author.
E-mail addresses: zzhh@hpu.edu.cn (Z. Zeng), 1612962996@qq.com (Y.Li)

so that it can detect any type of faults in distribution networks.

1.2 Issues of existing fault detection methods

Although a variety of methods have been produced, their actual detection effect is still difficult to meet the requirements, and there are certain shortcomings.

Feature extraction aspects: Most of the available detection measures use a fixed basis function to characterize the fault signal, which is not adaptive in the process of feature selection. HHT is adaptive. But the Intrinsic mode function (IMF) components generated by it are easy to modal aliasing.

Detection criterion aspects: Available fault detection criterion mostly use artificial neural network and other measures. Although they improve the accuracy of fault discrimination, its algorithm is complex. And the calculation time is long, and it relies on data samples. In order to ensure the completeness of the physical characteristics of the fault, some of the methods use dual-terminal quantities as fault characteristics, but for long-distance lines, the communication delay needs to be considered.

Algorithm performance: In the presence of high resistance, noise interference, lightning interference and other working conditions. They will cause the fault signal characterization of the fault information is missing. It is detrimental to the fault feature selection, leading to misjudgment.

1.3 Contributions

The main contributions of this paper for the problems raised above are as follows:

1) For the problem of feature extraction, it is proposed to adopt Aquila Optimizer (AO) to optimize CEEMDAN for fault feature extraction. CEEMDAN performs Empirical mode decomposition (EMD) decomposition by adding certain Gaussian white noise to the original signal. The frequency range of each IMF component obtained by decomposition expands with the addition of white noise. It effectively solves the modal aliasing problem. Compared with fixed basis function of WT and S-transform, CEEMDAN decomposition adopts an adaptive strategy in the construction of random noise to realize the control of noise size and distribution, which makes the signal decomposition results more accurate and stable. And the CEEMDAN optimal parameters are obtained by AO algorithm, which makes its extracted feature information richer.

2) Firstly, the percentage change of single-ended transient line mode current is calculated as the protection activation criterion. After determining the fault state, to decompose the single-ended fault current signal by CEEMDAN to get the IMF components of each order. Secondly, the internal and external fault criteria were built by calculating their energy moment eigenvalues. Thirdly, the proportion of the singular values of the first-order IMF(IMF_1) components of the fault current signals is employed to determine the fault pole. This protection algorithm is easily calculated, requires short time, and can obviously distinguish various fault types.

3) Through a large number of simulation verification, in the end of high resistance, noise interference, sampling frequency, current-limiting reactance size, lightning interference and other working conditions, fault detection and identification remain highly accurate.

The rest of the paper is organized as follows. In Sect. 2, the transient current fault characteristics of DC lines are analyzed. In Sect. 3, the fault feature acquisition method is introduced. In Sect. 4, the fault criterion is presented. The algorithm test validation is given in Sect. 5. The whole paper is summarized in Sect. 6.

2. Characterization of faults in Flexible DC distribution network

2.1 Topological structure

The equivalent model of the four-terminal flexible DC distribution network with MMC is shown in Fig. 1. Among them, MMC1~MMC4 are converter stations. AC System represents the AC system connected to the four-port converter station. DC circuit breakers and current limiting reactors are mounted at two ends of the DC line [19]. The internal pole-to-ground fault and the pole-to-pole fault at t line12 point f_1. f_2 is the forward external fault. f_3 is the reverse external fault.

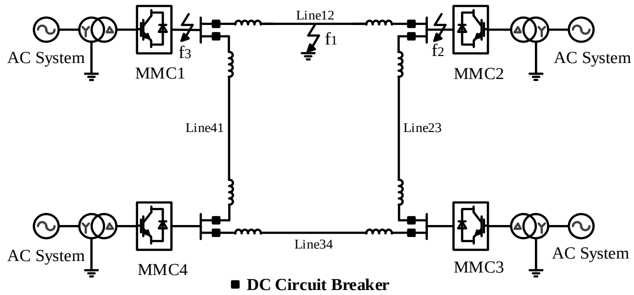

Fig. 1. Equivalent model of four terminal flexible DC distribution network

2.2 Characterization of fault transients internal and external to the zone

To analyze the transient features of the fault current of the DC line, a fault equivalent circuit diagram is drawn in this paper, as shown in Fig. 2. Z_{line1} and Z_{line2} are the equivalent impedances on two sides of fault location, respectively. Z_L is the impedance of current-limiting reactor. Z_{MMC1} and Z_{MMC2} are the equivalent impedances of the MMC1 and MMC2 converter stations. R_f is the transition resistance impedance. U_f is the additional power supply at the time of fault. gg is the measurement point of positive protection. P_a and P_b are the positive protection measurement points. N_a and N_b are the negative protection measurement points.

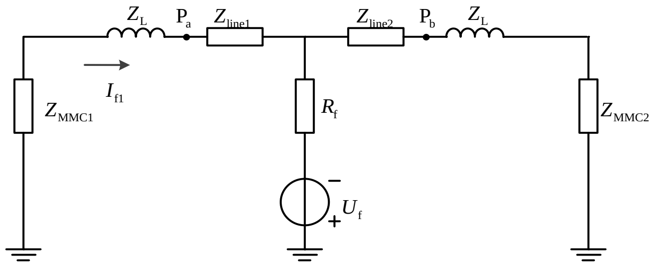

(a) Equivalent circuit diagram for monopole grounding fault in the f_1

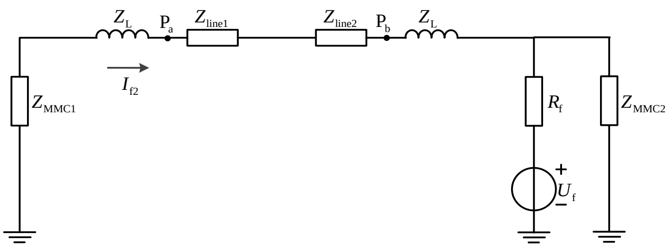

(b) Equivalent circuit diagram for monopole grounding fault in the f_2

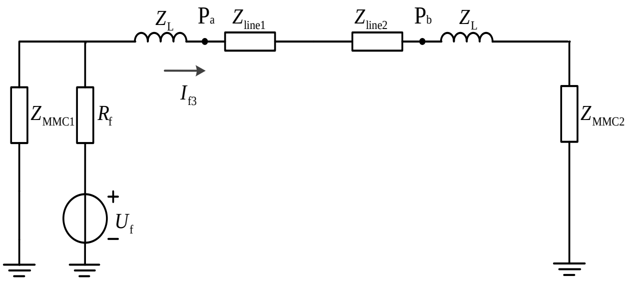

(c) Equivalent circuit diagram for monopole grounding fault in the f_3

Fig. 2. Equivalent circuit diagram of internal and external faults

From Fig.2, the expression for fault current in the internal fault is derived as:

$$I_{\mathrm{f1}} = \frac{U_{\mathrm{dc}}}{R_{\mathrm{f}} + Z_{\mathrm{line1}} + Z_{\mathrm{MMC1}} + Z_{\mathrm{L}}} \tag{1}$$

The expression for positive external fault current is:

$$I_{\mathrm{f2}} = \frac{U_{\mathrm{dc}}}{R_{\mathrm{f}} + \left(Z_{\mathrm{line1}} + Z_{\mathrm{line2}} + 2Z_{\mathrm{L}} + Z_{\mathrm{MMC1}}\right) // Z_{\mathrm{MMC2}}} \cdot \frac{Z_{\mathrm{MMC2}}}{Z_{\mathrm{line1}} + Z_{\mathrm{line2}} + 2Z_{\mathrm{L}} + Z_{\mathrm{MMC1}} + Z_{\mathrm{MMC2}}} \tag{2}$$

The expression for the reverse external fault current is:

$$I_{\mathrm{f3}} = \frac{U_{\mathrm{dc}}}{R_{\mathrm{f}} + \left(Z_{\mathrm{line1}} + Z_{\mathrm{line2}} + 2Z_{\mathrm{L}} + Z_{\mathrm{MMC2}}\right) // Z_{\mathrm{MMC1}}} \cdot \frac{Z_{MMC1}}{Z_{\mathrm{line1}} + Z_{\mathrm{line2}} + 2Z_{\mathrm{L}} + Z_{\mathrm{MMC1}} + Z_{\mathrm{MMC2}}} \tag{3}$$

Where: I_{f1}, I_{f2} and I_{f3} are the currents of internal fault, forward external fault and reverse external fault.

Find and simplify the ratio of internal to external fault currents respectively:

$$\frac{I_{\mathrm{f1}}}{I_{\mathrm{f2}}} = \frac{R_{\mathrm{f}} \cdot \left(Z_{\mathrm{line1}} + Z_{\mathrm{line2}} + 2Z_{\mathrm{L}} + Z_{\mathrm{MMC1}} + Z_{\mathrm{MMC2}}\right)}{Z_{\mathrm{MMC2}} \cdot \left(R_{\mathrm{f}} + Z_{\mathrm{line1}} + Z_{\mathrm{L}} + Z_{\mathrm{MMC1}}\right)} + \frac{Z_{\mathrm{MMC2}} \cdot \left(Z_{\mathrm{line1}} + Z_{\mathrm{line2}} + 2Z_{\mathrm{L}} + Z_{\mathrm{MMC1}}\right)}{Z_{\mathrm{MMC2}} \cdot \left(R_{\mathrm{f}} + Z_{\mathrm{line1}} + Z_{\mathrm{L}} + Z_{\mathrm{MMC1}}\right)} \tag{4}$$

$$\frac{I_{\mathrm{f1}}}{I_{\mathrm{f3}}} = \frac{R_{\mathrm{f}} \cdot \left(Z_{\mathrm{line1}} + Z_{\mathrm{line2}} + 2Z_{\mathrm{L}} + Z_{\mathrm{MMC1}} + Z_{\mathrm{MMC2}}\right)}{Z_{\mathrm{MMC1}} \cdot \left(R_{\mathrm{f}} + Z_{\mathrm{line1}} + Z_{\mathrm{L}} + Z_{\mathrm{MMC1}}\right)} + \frac{Z_{\mathrm{MMC1}} \cdot \left(Z_{\mathrm{line1}} + Z_{\mathrm{line2}} + 2Z_{\mathrm{L}} + Z_{\mathrm{MMC2}}\right)}{Z_{\mathrm{MMC1}} \cdot \left(R_{\mathrm{f}} + Z_{\mathrm{line1}} + Z_{\mathrm{L}} + Z_{\mathrm{MMC1}}\right)} \tag{5}$$

According to equations (4) and (5), the internal fault current is bigger than the external fault current. The amplitude fluctuation of the internal fault current is larger than the external fault. Therefore, the transient energy of the internal fault current is larger. And a suitable fault criterion can be constructed by utilizing this fault characteristic.

2.3 Analysis of transient characterization of internal faults

When a pole-to-ground fault occurs, electromagnetic coupling occurs between the positive and negative poles. The currents can be decoupled using Karrenbauer transform. Then the line-mode and zero-mode current components are acquired. The zero-mode component is propagated through the earth and can't form a loop current between the poles. So, it exists only for the pole-to-pole fault [20].

$$\begin{cases} \begin{bmatrix} i_1 \\ i_0 \end{bmatrix} = \dfrac{\sqrt{2}}{2} \begin{bmatrix} 1 & -1 \\ 1 & 1 \end{bmatrix} \begin{bmatrix} i_p \\ i_n \end{bmatrix} \\ \begin{bmatrix} i_p \\ i_n \end{bmatrix} = \dfrac{\sqrt{2}}{2} \begin{bmatrix} 1 & 1 \\ -1 & 1 \end{bmatrix} \begin{bmatrix} i_1 \\ i_0 \end{bmatrix} \end{cases} \tag{6}$$

Where: i_p and i_n are the positive and negative currents on the DC line. i_p is the zero-mode current and i_n is the line-mode current.

In order to analyze the positive and negative current fault characteristics during the internal fault, the line mode and zero mode network diagrams are constructed, as indicated in Fig. 3(a) and (b).

Among them, L_{pa} and L_{na} are the current limiting inductance L_{dc} on the positive and negative DC lines respectively. L_{line1} and L_{line2} are the equivalent inductance on the two sides of the fault point. L_{MMC1} and L_{MMC2} are the equivalent inductance of MMC1 and MMC2 converter stations. U_{f_1} and U_{f_0} are the additional power supply for line mode and zero mode faults. U_{MMC1} and U_{MMC2} are the voltage U_{dc} at the initial juncture of fault. Taking the direction of outflow from the bus as positive, I_{f_1} and I_{f_0} are the equivalent line mode and zero mode currents from the bus, respectively.

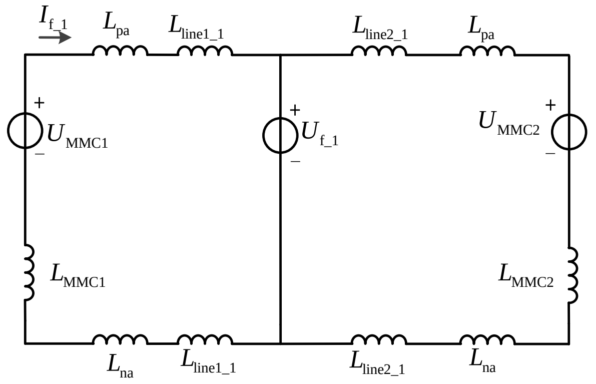

(a) Equivalent line mode network diagram of the internal monopole grounding fault

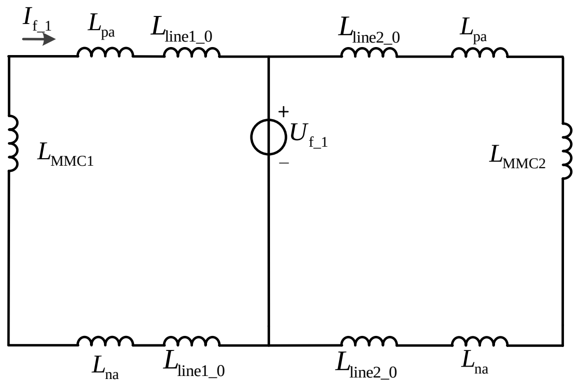

(b) Equivalent zero mode network diagram of the internal monopole grounding fault

Fig. 3. Equivalent network diagram of the internal monopole grounding fault.

Solving the equivalent network diagram for the internal pole-to-ground fault from the boundary conditions gives i_p and i_n :

$$\begin{cases} L_1 = 2L_{dc} + L_{MMC1} + 2L_{line1\_1} \\ L_2 = 2L_{dc} + L_{MMC2} + 2L_{line2\_1} \\ L_3 = 2L_{dc} + L_{MMC1} + 2L_{line1\_0} \\ L_4 = 2L_{dc} + L_{MMC2} + 2L_{line2\_0} \\ L_5 = L_3 // L_4 // L_1 \\ L_6 = L_3 // L_4 // L_2 \end{cases} \tag{7}$$

$$\begin{cases} i_p = \dfrac{\sqrt{2}}{2}\left[\dfrac{U_{dc}}{L_1+L_6}\cdot\left(1+\dfrac{L_6}{L_3}\right)+\dfrac{U_{dc}}{L_2+L_5}\cdot\left(\dfrac{L_5}{L_3}-\dfrac{L_5}{L_1}\right)\right] \\ i_n = \dfrac{\sqrt{2}}{2}\left[\dfrac{U_{dc}}{L_1+L_6}\cdot\left(\dfrac{L_6}{L_3}-1\right)+\dfrac{U_{dc}}{L_2+L_5}\cdot\left(\dfrac{L_5}{L_3}+\dfrac{L_5}{L_1}\right)\right] \end{cases} \tag{8}$$

According to Eq. (8), the difference between i_p and i_n at fault time is:

$$i_p - i_n = \frac{\sqrt{2}U_{dc}}{\left(L_1+L_6\right)} - \frac{\sqrt{2}U_{dc}}{\left(L_2+L_5\right)}\cdot\frac{L_5}{L_1} \tag{9}$$

According to Eq. (9), when the internal positive fault occurs: $i_p > i_n$ .Negative faults are based on the same principles as positive faults. So, when the internal negative ground fault occurs, $i_p < i_n$. However, the positive and negative electrical quantities of pole-to-pole fault are symmetrical and only line mode parts are present. So, the positive and negative currents: $i_p = i_n$. This difference in fault features between positive and negative currents can be utilized to construct an internal fault criterion.

The above analysis has proved that when the internal fault occurs, the DC line positive and negative currents i_p, i_n are different in amplitude size. Considering that the fault current signal is mostly a high-frequency component. The fault has the more obvious influence on the frequency domain characteristics. This paper continues to analyze its spectral characteristics by extracting them using the FFT transform, and the spectral waveforms are shown in Fig. 4.

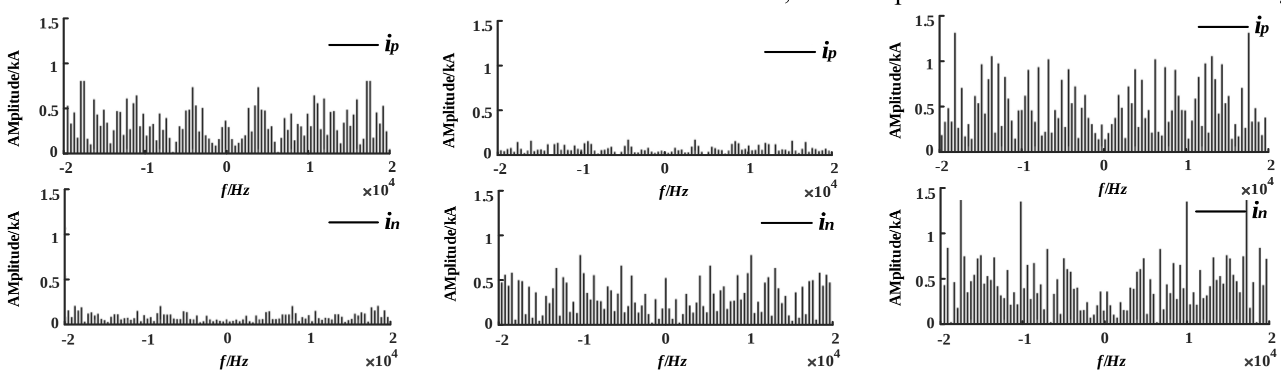

(a) Internal positive pole fault (b) Internal negative pole fault (c)Internal pole-to-pole fault

Fig. 4. Frequency spectrum of positive and negative fault currents

From Fig. 4:

1) When internal positive fault occurs, the amplitude magnitude of the positive fault current i_p with frequency fluctuation is obviously larger than that of the negative fault current i_n.

2) When the internal negative fault occurs, the magnitude of the positive fault current i_p with frequency fluctuation is significantly smaller than the negative fault current i_n.

3) When the internal pole-to-pole fault occurs, the amplitude fluctuations of i_p and i_n are similar.

The literature [25] has confirmed that the singular value produced by a certain frequency in the singular value vector is directly proportional to the magnitude size of the frequency in the magnitude spectrum. This paper adopts this conclusion. And based on the above analysis of the differences in the spectral characteristics of i_p and i_n under different operating conditions. The IMF singular value is taken as the fault feature quantity to construct the pole selection criterion in the zone.

3. Fault feature extraction method

3.1 CEEMDAN decomposition

CEEMDAN improves on EMD. It draws on the idea that the EEMD algorithm superimposes Gaussian white noise multiple times and integrally averages the intrinsic mode functions to eliminate the noise [21]. Thus, the modal aliasing is suppressed and better convergence is achieved. Since the decomposition process is completely advanced by the data, it is highly adaptive. The specific decomposition principle is as follows:

Step 1: Let S(n) be the original signal, and use EMD to decompose $S(n)=S(n)+W_i$ (i=1,2, ..., I), where W_i is the added white noise, to obtain the IMF_1:

$$\mathrm{IMF}_1=\frac{1}{I}\sum_{i=1}^{I}\mathrm{IMF}_{i1} \tag{10}$$

where: IMF_1 is the first-order eigenmode component, IMF_{i1} is the ith eigenmode component. I is the times that white noise is added.

Step 2: Calculate the first margin:

$$r_1^{(n)}=S(n)-IMF_{i1} \tag{11}$$

Step 3: Next, the signal $r_1(n)+\varepsilon E_1(W_i(n))$ is decomposed by EMD. Where: E_a is the ath modal component after EMD decomposition, and ε is the adaptive coefficient, to obtain IMF_2:

$$\mathrm{IMF}_2=\frac{1}{I}\sum_{i=1}^{I}E_1\left(r_1(n)+\varepsilon E_1\left(W_i(n)\right)\right) \tag{12}$$

Step 4: Calculate the ath remainder $r_a(n)$:

$$r_a^{(n)}=r_{a-1}^{(n)}-\mathrm{IMF}_a, \tag{13}$$

Step 5: Calculate the a+1st CEEMDAN modal component:

$$\mathrm{IMF}_{a+1}=\frac{1}{I}\sum_{i=1}^{I}E_1\left(r_a(n)+\varepsilon E_a\left(W_i(n)\right)\right) \tag{14}$$

Step 6: Repeat steps 4~5 until the residual residue cannot be decomposed any further to obtain a residue of R(n).

3.2 Improvement of CEEMDAN

AO achieves the purpose of optimality seeking by simulating the four behavioral states in the process of capturing prey by skyhawk. It has more outstanding performance in convergence speed and optimization seeking effect [22]. Specifically divided into the following four behavioral states:

Step 1: Expanding the Search

The Aquila is in a vertically curved, high-flying state and mathematical modeling is as follows:

$$X_1(t+1)=X_{\mathrm{M}}(t)\times\left(1-\frac{t}{T}\right)+\left(X_{\mathrm{a}}(t)-X_{\mathrm{M}}(t)*\mathrm{rand}\right) \tag{15}$$

$$X_{\mathrm{a}}(t)=\frac{1}{N}\sum_{i=1}^{N}X_i(t),\forall j=1,2,\cdots,\mathrm{Dim} \tag{16}$$

Where: aa is the solution of the t+1st iteration of method X_1. bb is the optimal solution before the tth iteration. cc is the average value of the solution of the tth iteration. Rand is a random number between 0 and 1. N is the population size. Dim is the number of optimization variables. T and t stand for the current number of iterations and the maximum number of iterations, respectively.

Step 2: Narrowing the search

Aquila is in short glide attack flight and mathematical modeling is as follows:

$$L_{\mathrm{evy}}(D)=s\times\frac{q\times\sigma}{|p|^{\frac{1}{\beta}}} \tag{17}$$

$$\sigma=\left(\frac{\Gamma(1+\beta)\times\sin\left(\frac{\pi\beta}{2}\right)}{\Gamma(\frac{1+\beta}{2})\times\beta\times 2\left(\frac{\beta-1}{2}\right)}\right)^{\frac{1}{\beta}} \tag{18}$$

Where: $L_{\mathrm{evy}}(D)$ is the flight distribution function. q and p are random numbers obeying N $(0,\sigma^2)$ and N (0,1) Gaussian distributions, respectively. β is a fixed value of 1.5, and Γ is the gamma function.

$$\theta=-\omega\times D_1+\frac{3\pi}{2} \tag{19}$$

$$r=r_1+\mathrm{U}\times D_1 \tag{20}$$

Where: θ is the helix angle, r is the helix radius, r1 is the search period, U takes the value 0.00565, and D_1 is an integer between [1, Dim].

$$\begin{aligned}X_2(t+1)=&X_{\mathrm{M}}(t)\times L_{\mathrm{evy}}(D)+X_{\mathrm{r}}(t)\\&+\left(r\times\cos(\theta)-r\times\sin(\theta)\right)*\mathrm{rand}\end{aligned} \tag{21}$$

where: $X_2(t+1)$ is the solution at the t+1st iteration of method X_2 and $X_{\mathrm{r}}(t)$ is the solution between [1, N] at the tth iteration.

Step 3: Expanded Development

The Aquila is in a low altitude, slow descending attack flight and its mathematical model is as follows:

$$\begin{aligned}X_3(t+1)=&\left(X_{\mathrm{M}}(t)-X_a(t)\right)\times\alpha-\mathrm{rand}\\&+\left((\mathrm{UB}-\mathrm{LB})\times\mathrm{rand}+\mathrm{LB}\right)\times\delta\end{aligned} \tag{22}$$

Where: $X_3(t+1)$ is the solution of the t+1st iteration of method X_3. α and δ are fixed values 0.1. UB, LB are the top and bottom limits of the proposed problem.

Step 4: Narrowing down the exploitation

The Aquila is in the state of land walking to capture prey and its mathematical model is as follows:

$$\begin{cases} QF(t) = t^{\frac{2\times \text{rand}-1}{(1-T)^2}} \\ K_1 = 2\times \text{rand} - 1 \\ K_2 = 2\times\left(1-\dfrac{t}{T}\right) \end{cases} \tag{23}$$

Where: QF(t) is the equilibrium search quality function for t iterations, K_1 is the various motions of the AO, and K_2 is the flight rate of the AO. T and t are the maximum iteration number and the current iteration number.

$$X_4(t+1) = QF(t)\times X_M(t) - \left(K_1\times X(t)\times \text{rand}\right) - K_2\times L_{evy}(D) + \text{rand}\times K_1 \tag{24}$$

where: $X_4(t+1)$ is the solution for the t+1st iteration of method X_4.

Since the feature extraction effect of CEEMDAN algorithm depends on the white noise amplitude weight (Nstd) and the number of noise additions (NE). AO is used to optimize the 2 parameters of CEEMDAN. The minimum envelope entropy is the fitness function. The lower the value of fitness, the greater the decomposition. And the richer the feature extraction. The detailed steps of AO-CEEMDAN are as follows:

1) Set the parameters of AO like the iteration number, population number, UB and LB.

2) Decompose signal using CEEMDAN to obtain the eigenmode components of each order.

3) Calculate the minimum envelope entropy of each order IMF component.

4) Constantly update the population position. Stop the iteration when the minimum of envelope entropy is reached, and then export the optimal parameters.

3.3 AO-CEEMDAN parameter settings

Set the number of AO populations to 10, the maximum of iterations to 20, the upper and lower bounds of Nstd to [0.15, 0.6], and the top and bottom limits of NE to [50, 800].

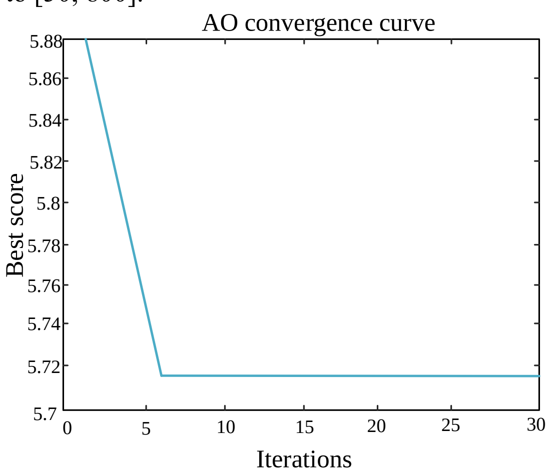

Fig. 5. AO Iterative Optimization CEEMDAN

Through simulation experiments, it is concluded that the minimum envelope entropy is obtained when the iteration reaches the 6th time. Meanwhile, the optimal parameter [Nstd, NE] is [0.15046, 584], and its optimization curve is shown in Fig. 5.

4. Fault Identification Methods

4.1 The starting criterion

When the system is in the normal state, the DC line mode current remains in a stable state. When the system fault happens, the fault line mode current rises rapidly, has obvious fluctuations and produces large sudden changes. In this paper, this transient feature is utilized, and the transient line mode current change rate is adopted as the starting criterion, whose expression is:

$$K_1 = \left|\frac{di_1}{dt}\right| \geq K_{\text{set1}} \tag{25}$$

Where: K_1 is the transient line mode current rate of change of line 12. K_{set1} is the transient line mode current rate of change threshold. The principle of rectification is set to avoid the maximum value of the transient line mode current change rate in normal state. According to the simulation test, the selected rectification value is 0.9kA/ms, and after considering a certain margin, the selected startup data time window is 0.5ms.

To avoid the effect of lightning strike interference, it is necessary to set the threshold of lightning strike interference. Due to the difference between the high and low frequency energies of the transient current generated by the lightning wave during lightning interference. The low frequency energy accounts for a smaller proportion and the high frequency energy accounts for a larger proportion [24]. Therefore, the ratio of high and low frequency energy of the transient line mode current is selected to construct the lightning strike interference criterion.

$$\beta = \frac{E_{\text{a}}}{E_{\text{d}}} > \beta_{set} \tag{26}$$

Where: β is the ratio of high and low frequency energy of transient line mode current. β_{set} is the threshold value of lightning interference. E_a is the high frequency energy of transient line mode current, and E_d is the low frequency energy of transient line mode current. Through simulation verification, in the time window of 0.2ms to take a specific margin. And the selected value of 2.

4.2 Criterion for internal and external faults

According to the fault characterization in section 2.2, when different faults occur in the system, there is marked discrepancy in the fault current size of the DC line. The IMF energy moment adds the time factor to traditional feature extraction methods such as IMF energy and energy entropy, which better reflects the distribution characteristics of energy on the time scale and represents deeper feature information [19]. Therefore, the IMF energy moment of i_p can be taken to discriminate internal and external faults. The steps for constructing the criterion are as follows:

Step 1: Calculate the first-order difference for $i_{\mathrm{p}}(t)$ to add the characteristic difference.

$$i_{\mathrm{pd}}(t) = diff\left(i_{\mathrm{p}}(t)\right) \tag{27}$$

Where: $i_{\mathrm{pd}}(t)$ is the result of the first-order difference of $i_{\mathrm{p}}(t)$, and $i_{\mathrm{p}}(t)$ is the DC line positive current at the time of fault.

Step 2: Perform CEEMDAN decomposition on $i_{\mathrm{pd}}(t)$ to obtain the IMF components of each order.

Step 3: Calculate the energy moments of the processed 1st to 4th order IMF components, and then calculate the energy moment eigenvalue E_l, which is the logarithms of their total values.

$$E_i = \sum_{j=1}^{N} (j\Delta t)\left|H_i(j\Delta t)\right|^2, (i = 1,2,3,4) \tag{28}$$

$$E_l = \ln\left(\sum_{i=1}^{4} E_i\right) \tag{29}$$

Where: E_i is the ith order IMF energy moment and N is the number of sampling points. Δt is the sampling period, and $H_i(j)$ denotes the amplitude of the ith order IMF component at the jth discrete point.

The positive fault current in the 2ms time window is selected as the original signal. The 1~4th order IMF energy moments eigenvalues calculated through the above steps , and their values are printed in Table 1.

Table 1 IMF1 Energy Values during Internal and External Faults in Zone 2

Fault Type	E_l
Internal positive pole-to-ground fault	1.1407
Internal negative pole-to-ground fault	1.3462
Internal pole-to-pole fault	1.8963
Positive external fault	-0.3743
Reverse external fault	-0.4953

From Table 1, when the internal fault occurs, the E_l of the positive fault current i_{p} is greater than 0; when external fault occurs, the E_l of i_p is less than 0. Therefore, the following internal and external fault criteria can be constituted by Eq. (30):

$$\begin{cases} E_l > 0 & \text{Internal fault} \\ E_l < 0 & \text{External fault} \end{cases} \tag{30}$$

4.3 pole-selection criterion

On the basis of the analysis in section 2.3, when positive, negative and pole-to-pole faults happen, there is a discrepancy in the size of the positive and negative pole fault currents. By utilizing this fault characteristic, pole selection criteria can be established using singular values. The detailed steps are as follows:

Step 1:Firstly, CEEMDAN is used to decompose the i_p and i_n signals and extract the first-order intrinsic modal component IMF1.

Step 2:The decomposed IMF1 signal is integrated once to highlight the fault characteristics.

Step 3:Calculate the IMF1 matrix singular values, and the resulting singular value data is shown in Table 2.

$$\begin{cases} A = USV^H \\ S = \begin{pmatrix} \Sigma\, 0 \\ 0\, 0 \end{pmatrix} \\ \Sigma = \mathrm{diag}\left(\delta_1, \delta_2 \cdots \delta_r\right) \end{cases} \tag{31}$$

Where: A is the IMF1 matrix, U and V are the unitary matrix, and $\delta_1 \geq \delta_2 \geq \cdots \geq \delta_r > 0$ is the singular value of matrix A.

Table 2 Singular values of IMF_1 for internal faults

Fault Type	S_{ip}	S_{in}	S_{ip}/S_{in}
Internal positive pole fault	67.3504	3.3628	20.0281
Internal negative pole fault	2.5257	93.7329	0.0269
Internal pole-to-pole fault	80.3109	128.4304	0.6253

According to Table 2, when the internal positive pole fault happens, $S_{ip} > S_{in}$. When the internal negative pole fault occurs, $S_{ip} < S_{in}$. When the pole-to-pole fault happens, $S_{ip} \approx S_{in}$.

Define K_2 as the ratio of the singular value of positive and negative pole fault current IMF1.

$$k_2 = \frac{S_{\mathrm{ip}}}{S_{\mathrm{in}}} \tag{32}$$

Where: S_{ip} is the singular value of the positive fault current, and S_{in} is the singular value of the negative fault current.

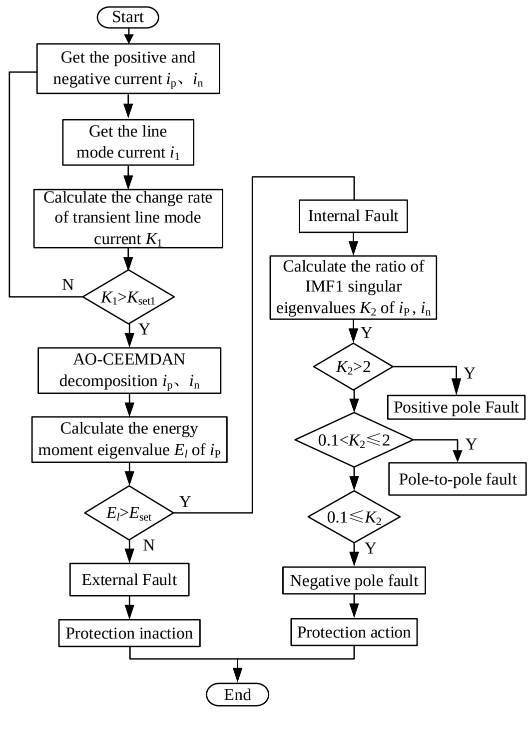

Fig. 6. Protection Scheme Flowchart

Considering a certain margin and defining the reliability coefficients K_{set21} as 2 and K_{set22} as 0.1. The following criterion can be constituted:

$$\begin{cases} K_2 > 2 & \text{positive pole fault} \\ 0.1 < K_2 \le 2 & \text{pole-to-pole fault} \\ K_2 \le 0.1 & \text{negative pole failure} \end{cases} \tag{33}$$

In summary, the flow of the fault protection method for Flexible DC distribution network on the basis of difference of fault current transient characteristics is shown in Fig. 6.

5. Simulation Verification

The model of four-terminal flexible DC distribution network with MMC shown in Fig. 1 is established by PSCAD/EMTDC and simulated for validation. Among them, the sub-module adopts a half-bridge structure. The overhead line is modeled as frequency dependent. The system is a symmetrical unipolar system with constant DC voltage control for MMC1 and constant active power control for MMC2-MMC4. The sampling frequency of the system is 50kHz. The fault moment is 7s. The fault duration is 1s. And the length of the data window is 2ms. The simulation parameters are listed in Table 3.

Table 3 Simulation Parameters of Flexible DC System

Parameters	Value
MMC1 rated capacity/(MVA)	20
MMC2-MMC4 rated capacity/(MVA)	500
Rated DC voltage/kV	500
Sub-module capacitance/mF	15
Bridge arm inductance/mH	100
Number of half-bridge sub-modules	264
Line length/km	100

5.1 Simulation results inside and outside the area

The fault points f_1 is set at 10km, 50km and 90km away from the protection installation. The f_2 and f_3 fault points are located at the exit of the inverter station and rectifier station. The transition resistance values are 0.01Ω(metallic grounding), 100Ω and 300Ω, and the simulation results are presented in Table 4 and Fig. 7.

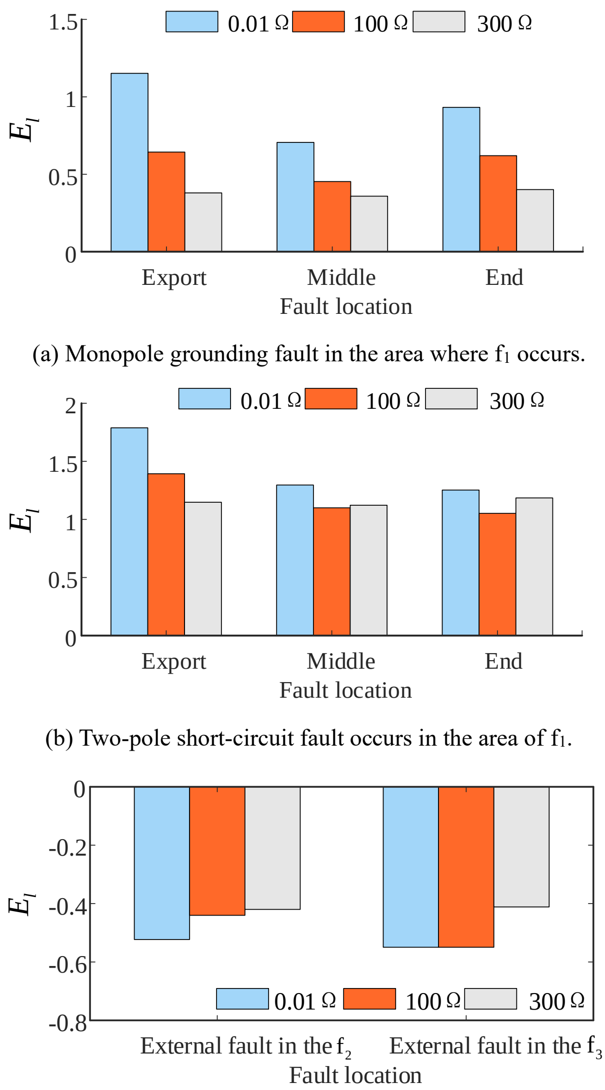

(a) Monopole grounding fault in the area where f_1 occurs.

(b) Two-pole short-circuit fault occurs in the area of f_1.

(c) Out-of-area unipolar grounding fault occurs at f_2 and f_3.

Fig. 7. E_l at different fault distances and transition resistances

Table 4 Fault Identification Results

Fault Type	Fault Location	Transition Resistance	K_1
Internal pole-to-ground fault in the f_1	10km from protection equipment	0.01	225
		300	116
	90km from protection equipment	0.01	2.96
		300	2.24
Internal pole-to-pole fault in the f_1	10km from protection equipment	0.01	482
		300	319
	90km from protection equipment	0.01	3.61
		300	3.15
External pole-to-ground fault in the f_2	Converter station exit	0.01	3.79
		300	2.07
External pole-to-ground fault in the f_3	Converter station exit	0.01	36
		300	2.31

From Table 4, when internal and external faults happen in the system, the K_1 within the 2ms time window meets the protection startup criterion. From Fig.7, when an internal fault happens at the fault point f_1, the E_l is greater than 0, which is determined to be an internal fault. The E_l of fault points f_2 and f_3 are all less than 0, which are judged as external faults and meet the internal and external criteria of protection.

5.2 Simulation results of fault pole selection

After judging that the DC line fault belongs to the internal fault, it is needed to continue to propose the fault pole selection criterion, and the simulation results are presented in Fig. 8.

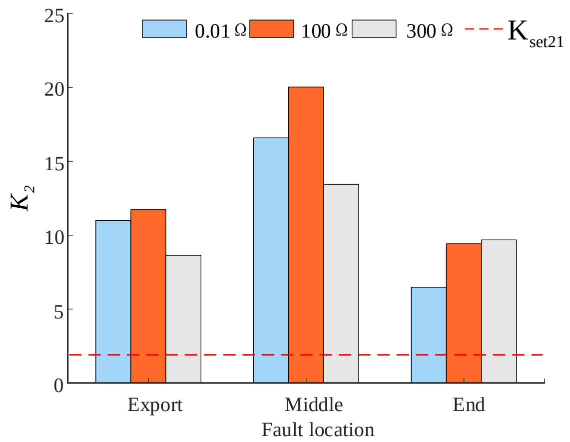

(a) Internal positive pole-to ground fault in the area where f_1 occurs.

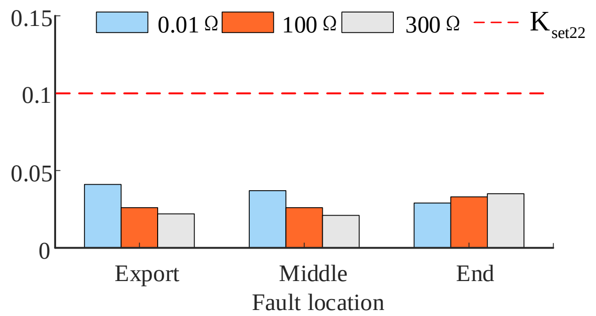

(b) Internal negative pole-to ground fault in the area where f_1 occurs.

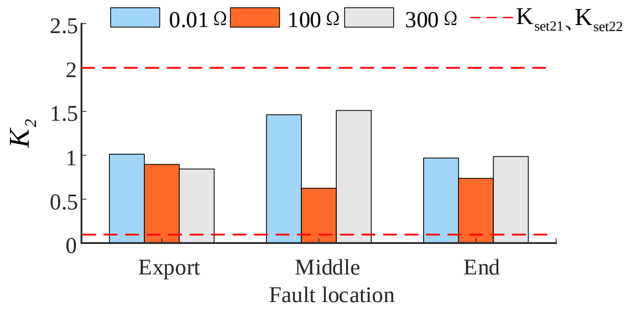

(c) Internal pole-to-pole fault in the area where f_1 occurs.

Fig. 8. K_2 at different fault distances and transition resistances

From Fig. 8:

1) When the positive fault happens, the ratio K_2 of the IMF_1 singular values of the positive fault current to the negative fault current is greater than K_{set21}.

2) When the negative fault happens, the ratio K_2 of the IMF_1 singular values is less than K_{set22}.

3) When the pole-to-pole fault happens, the ratio K_2 of the IMF1 singular values is between K_{set22} and K_{set21}.

Therefore, the protection method proposed can quickly and reliably identify the faulty pole under different operating conditions with multiple fault locations and transition resistances within a 2ms time window.

5.3 White noise test

To verify that the protection scheme proposed is still reliable when disturbed by noise. Therefore, a 20dB Gaussian white noise is added for simulation within 1ms after the system fault. And the simulation results when the transition resistance value is 300Ω are listed in Table 5.

Table 5 Simulation results of protection scheme under 20dB white noise interference

Fault Type	Fault Location	E_l	K_2	Fault Identification
Positive internal fault at point f_1	50km	0.3964	12.52	Internal positive pole fault
	90km	0.4605	10.05	Internal positive pole fault
Internal pole-to-pole fault at point f_1	50km	1.3328	0.81	Internal pole-to-pole fault
	90km	1.2186	0.85	Internal pole-to-pole fault
External pole-to-ground fault at point f_2	Inverter station exit	-0.4696		Positive external fault
External pole-to-ground fault at point f_3	Rectifier station exit	-0.3989		Reverse external fault

From Table 5, in the case where the system is disturbed by noise, the internal and external faults can still be rightly recognized and the fault poles can be accurately determined.

5.4 Test of current-limiting reactance

To minimize the effect of current increase when a fault occurs, a current-limiting reactor is usually connected in series on the DC line of the system. When the current limiting reactance increases, the fault current will decrease, and vice versa. Since this paper uses the fault current to construct the protection criterion, the size of the current-limiting reactance will have an impact on the protection reliability. To verify the impact of different current-limiting reactance on fault identification, the fault discrimination results of 0.15H current-limiting reactance, 300 transition resistance are given, as shown in Table 6.

Table 6 Simulation Results of Protection Scheme under 0.15H Current Limiting Reactance

Fault Type	Fault Location	E_l	K_2	Fault Identification
Positive internal fault at point f1	90km	0.4096	2.38	Internal positive pole fault
Internal pole-to-pole fault at point f1	90km	1.0477	0.90	Internal pole-to-pole fault

External pole-to-ground fault at point f2	Inverter station exit	-0.9015	Positive external fault
External pole-to-ground fault at point f3	Rectifier station exit	-1.2835	Reverse external fault

Table 6 shows that E_l and K_2 of different faults satisfy the internal and external fault criteria and the fault pole-selection criterion. This protection method can reliably recognize various fault types under the influence of different current-limiting reactance.

5.5 Sampling frequency test

The size of the sampling frequency affects the selection of sampling data, the higher the sampling frequency, the more sampling data. To verify the influence of different sampling frequencies on fault identification, the fault discrimination results under 25kHz sampling frequency and 300Ω transition resistance are given, as shown in Table 7.

Table 7. Simulation Results of Protection Scheme at 25kHz Sampling Frequency

Fault Type	Fault Location	E_l	K_2	Fault Identification
Positive internal fault at point f1	90km	0.6973	16.08	Internal positive pole fault
Internal pole-to-pole fault at point f1	90km	1.3254	1.20	Internal pole-to-pole fault
External pole-to-ground fault at point f2	Inverter station exit	-0.2037		Positive external fault
External pole-to-ground fault at point f3	Rectifier station exit	-0.2101		Reverse external fault

According to Table 7, the method of this paper can still reliably recognize various fault types for the sampled data at 25kHz sampling frequency.

5.6 Lightning interference test

Considering that this paper adopts the transient line mode current rate of change as the criterion for protection activation, and lightning interference will cause overcurrent resulting in protection mis-activation. Therefore, it is needed to discuss the anti-lightning interference influence of the protection scheme in this paper. Figure 7 shows the lightning current model with 2.6/50μs double exponential wave. The fault discrimination results are given when a lightning strike disturbance with an amplitude of 20kA occurs, as shown in Table 9.

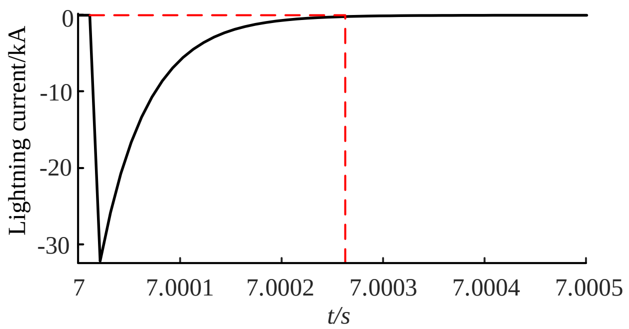

Fig. 9. Lightning current waveform

Table 8. Simulation results of protection schemes under lightning interference

Fault Type	Fault Location	β
f_1	Lightning interference	5.0274
	Ground fault	1.9858
f_2	Lightning interference	4.5967
	Ground fault	1.1619
f_3	Lightning interference	4.0347
	Ground fault	0.1967

According to Table 8, when lightning interference occurs at different locations of the line, β is greater than β_{set}, so it can effectively recognize the lightning interference and the protection is reliably inoperative.

5.7 Comparisons with other methods

5.7.1 Comparison with protection schemes based on signal decomposition algorithms

Existing literatures have proposed decomposition algorithms based on VMD, CEEMD, and others as fault signal feature extraction methods.To further demonstrate the feasibility and superiority of CEEMDAN data processing, VMD and CEEMD processing data are substituted into the protection scheme under high resistance conditions at the end of the DC line. The results are listed in Table 9.

Table 9. Simulation results of fault pole selection under high terminal resistance

Transition resistance /Ω	E_l		
	CEEMDAN	VMD	CEEMD
0.01	0.6710	1.3224	1.5645
	0.7412	1.3565	1.6602
	1.3035	1.8240	2.4147
	-0.3698	0.8139	1.4276
	-0.5066	0.3982	0.7664
500	0.1780	0.3214	0.7501
	0.2069	0.3554	0.8617
	0.8592	0.5652	1.8142
	-0.9674	-0.5147	0.6040
	-1.0395	-0.5269	-0.2395

According to Table 9, it can be seen that: comparing with the use of VMD and CEEMD, the CEEMDAN is more discriminating to the fault type. Its fluctuation trend is relatively flat with the increase of transition resistance. It is less affected by the value of transition resistance. So, it has a strong resistance to transition resistance in the case of high resistance at the end. The VMD and CEEMD algorithms, on the other hand, will have discrimination errors as the resistance value increases, indicating that such decomposition algorithms cannot adapt to long-distance and high transition resistance conditions.

5.7.2 Comparison with protection schemes based on current transients

The existing literature proposed an internal and external fault discrimination criterion method based on current fluctuation amplitude [26]. In this literature, the fault locations are limited to different lines in the grid. The situation of external metallic ground faults occurring close to the converter station location is not considered. Moreover, the performance analysis of the protection scheme does not consider the effect on the current transient quantity when the current limiting reactor L_{dc} is increased and the fault currents in the zone and outside the zone are reduced. The protection method proposed in this paper is simulated in different fault locations, current-limiting reactance size and other conditions, and the results show that they can accurately identify the type of fault.

6. Conclusion

This paper proposed a multi-port flexible DC distribution network fault protection method based on the difference of fault current transient features. The protection performance of the proposed method is verified by simulation tests:

1) This paper analyzed in detail the differences in DC line fault currents during internal and external faults, as well as the magnitude of fault currents between the fault pole and the sound pole during an internal fault. It provides a reliable theoretical basis for the development of the protection method.

2) The AO-CEEMDAN algorithm is utilized in signal decomposition with the advantages of self-adaptation and elimination of modal aliasing to find the optimal parameters and achieve the best decomposition effect, and combined with the characteristics of the IMF energy moment eigenvalues and singular values that have obvious differences under different faults, fault feature extraction is carried out. This paper selected a variety of electric quantity to construct fault criterion, which makes the fault characteristic difference more obvious. By using single-end volume data to eliminate the effect of communication delay, and the data window is set to 2ms, so the protection has good reliability and sensitivity.

3) Verified by simulation, this method still has good protection performance and resistance to transition resistance and noise interference under the following working conditions: different fault locations, different sampling frequencies, high resistance, thunder interference, different current-limiting reactance and noise effects.

Acknowledgement

This work is supported by the National Natural Science Foundation of China (Grants No. 61703144 and No.52177114).

Reference

[1] LI Bin, HE Jiawei, TIAN Jie, et al. DC fault analysis for modular multilevel converter-based system[J]. Journal of Morden Power System and Clean Energy, 2017, 5(2): 275-282.

[2] K. Jia, Z. Xuan, T. Feng, C. Wang, T. Bi and D. W. P. Thomas: Transient High-Frequency Impedance Comparison-Based Protection for Flexible DC Distribution Systems. IEEE Transactions on Smart Grid, vol. 11, no. 1, pp. 323-333, Jan. 2020.

[3] J. Suonan, S. Gao, G. Song, Z. Jiao and X. Kang: A Novel Fault-Location Method for HVDC Transmission Lines. IEEE Transactions on Power Delivery, vol. 25, no. 2, pp. 1203-1209, April 2010.

[4] C. Li, A. M. Gole and C. Zhao: A Fast DC Fault Detection Method Using DC Reactor Voltages in HVDC Grids. IEEE Transactions on Power Delivery, vol. 33, no. 5, pp. 2254-2264, Oct. 2018.

[5] M. Zhang, R. Guo and H. Sun: Fault Location of MMC-HVDC DC Transmission Line Based on Improved VMD and S Transform. 2020 4th International Conference on HVDC (HVDC), Xi'an, China, 2020, pp. 792-796.

[6] S. Mangalge and S. Jawale: Location of fault in long HVDC transmission line using continuous wavelet transform. 2016 International Conference on Signal Processing. Communication, Power and Embedded System (SCOPES), Paralakhemundi, India, 2016, pp. 930-935.

[7] Nanayakkara O, Rajapakse A, Wachal R: Traveling-wave-based line fault location in star-connected multiterminal HVDC systems. IEEE Trans. Power Deli, vol. 23, pp. 2286-2294, October 2012.

[8] X. Liu, A. H. Osman and O. P. Malik: Hybrid Traveling Wave/Boundary Protection for Monopolar HVDC Line. IEEE Transactions on Power Delivery, vol. 24, no. 2, pp. 569-578, April 2009.

[9] Xiang, S. Yang, L. Xu, J. Zhang, W. Lin, and J. Wen: A transient voltage-based DC fault line protection scheme for MMC-based DC grid embedding DC breakers. IEEE Trans. Power Del., vol. 34, no. 1, pp. 334–345, Feb. 2019.

[10] Chuanxin Xi, Qing Chen and Lei Wang: A single-terminal traveling wave fault location method for VSC-HVDC transmission lines based on S-transform. 2016 IEEE PES Asia-Pacific Power and Energy Engineering Conference (APPEEC), Xi'an, 2016, pp. 1008-1012.

[11] H. C. Shu and S. Y. Sun: A new method to detect single-phase fault feeder in distribution network by using S-transform. Proc. IEEE 11th Int. Conf. Probabilistic Methods Appl. Power Syst., 2010, pp. 277–282.

[12] Z. Li, G. Zou, T. Du and W. Yang: S-transform based pilot protection method for HVDC transmission lines. 2015 5th International Conference on Electric Utility Deregulation and Restructuring and Power Technologies (DRPT), Changsha, China, 2015, pp. 1667-1672.

[13] S. Luo, X. Dong, S. Shi and B. Wang: A Directional Protection Scheme for HVDC Transmission Lines Based on Reactive Energy. IEEE Transactions on Power Delivery, vol. 31, no. 2, pp. 559-567.

[14] Hao Y, Wang Q, Li Y, et al. An intelligent algorithm for fault location on VSC-HVDC system[J]. International Journal of Electrical Power & Energy Systems, 2018, 94:116-123.

[15] He J, Chen K, Li M, et al. Active injection protection scheme for flexible HVDC grids based on amplitude of input impedance[J]. GLOBAL ENERGY INTERCONNECTION-CHINA, 2021, 4(6):12.

[16] M. Li, K. Chen, J. He, Y. Tang and J. Tang: Impedance Phase

Based Active Injection Protection for Radial VSC-HVDC Grid. IEEE Transactions on Power Delivery, vol. 38, no. 3, pp. 1621-1635, June 2023.
[17]Yu S , Wang X , Zhang X P: A sensitive single-end DC line fault detection method for MMC-HVDC grids using reactor voltage ratio[J].International journal of electrical power and energy systems, 2023.
[18]M. A. Barik, A. Gargoom, M. A. Mahmud, M. E. Haque: A. M. T, Oo, and H. Al-Khalidi: Mathematical morphology-based fault detection technique for power distribution systems subjected to resonant grounding. Proc. IEEE Power Energy Soc. Gen. Meeting, Chicago, IL, USA:, 2017, pp. 1–5.
[19]Zhang Lishi, Liang Deliang, Liu Hua, et al. Fault identification of hybrid distribution transformers based on wavelet transform and logistic regression[J]. Journal of Electrical Technology, 2021,36 (S2): 467-476.
[20]Liu Keyan, Ren Zhaoying, Wang Yao: A Fault Location Method for Multi terminal Flexible DC Distribution Network Based on Control and Protection Collaboration[J]. High voltage technology, 2023, 49(08): 3458-3466.
[21]Yang Fan, Su Lei, Yang Zhichun, et al. Arc detection of series faults in low-voltage power supply lines based on improved CEEMDAN decomposition and spatiotemporal features[J]. Power System Protection and Control, 2022, 50 (12): 72-81.
[22]Liu Q, Cao N, Li M, et al. Wireless channel state prediction method based on improved adaptive and parameter-free recurrent neural structure[J]. IEEE Access , 2022, 10:6332.
[23]Wei Yanfang, Wang Zhijie, Wang Peng, et al. A Fault Protection Method for Flexible DC Distribution Networks Based on Current Limiting Reactance Voltage[J]. High voltage technology, 2022, 48(12): 5068-5079.
[24]Xing Chao, Huang Ze, Bi Guihong, et al. Research on Single End Directional Protection of UHV Three Terminal Hybrid DC Transmission Lines Based on Low Frequency Attenuation Characteristics in T-Zone and Directional Components [J/OL] Grid technology: 1-13 [2024-01-12].
[25]Li Hua, Liu Tao, Wu Xing, et al. The Application of SVD with Related Singular Value Ratio in Bearing Fault Diagnosis[J]. Journal of Mechanical Engineering, 2021, 57 (21): 13.
[26]Fu Hua, Liu Zhenmin, Chen Haoxuan, et al. Fault Identification of multi-terminal Flexible DC Transmission Lines Based on current transient[J]. Proceedings of the CSU-EPSA, 2022, 34(4): 107-115.